Research paper

Characterizing guanine's binding modes with potential Ru(II) monofunctional adducts: A local vibrational mode study

Hunter La Force, Elfi Kraka *

Computational and Theoretical Chemistry Group (CATCO), Department of Chemistry, Southern Methodist University, Dallas, TX 75275, USA

GRAPHICAL ABSTRACT

HIGHLIGHTS

• Proposes a series of complexes targeting DNA and their structure–activity profile.
• Features local mode analysis (LMA) in extracting local bond strength character.
• Compares local descriptors of LMA to global descriptors of bond dissociation energies.

ARTICLE INFO

ABSTRACT

We have investigated the bonding features of 18 Ruthenium(II) polypyridyl complexes of the type $[Ru(tpy)(L)-(Guo)]^{n+}$, containing a tridentate $2,2':6',2''$-terpyridine ligand (tpy) and various bidentate ancillary ligands L, which form monofunctional adducts with guanine derivatives, such as guanosine (Guo). The main scaffold is motivated by the work of Simović et al. (2019). These complexes have been proposed to form a covalent bond with the nucleobase Guanine at its N_7 position. This work illustrates the power of our local mode analysis in characterizing the strength of chemical interactions for experimentalists and theoreticians alike.

* Corresponding author.
E-mail address: ekraka@smu.edu (E. Kraka).

1. Introduction

Cancer is broadly known as the uncontrolled division of cells, but it is arguably better known as the second leading cause of death in the United States, despite delays in diagnosis onset by the COVID-19 pandemic [1]. Metal-based chemotherapies, such as cisplatin and its derivatives, have dominated the field of cancer therapeutics, with use in roughly 50%–70% of cancer treatments [2]. These drugs benefit from slow ligand exchange rates and two oxidation states that allow for various coordination geometries and ligands that can be further modified for solubility, target selectivity, and cytotoxicity [3]. These targets range from the prototypical cancer target, DNA, with drugs like cisplatin, [4] to proteins and transcription factors [5], as seen with oxaliplatin [6]. While these complexes exhibit a variety of frameworks and viable targets, platinum-based chemotherapies have attenuated bacterial resistance in some cancers [7]. In light of this, new metal complexes are needed to mitigate this bacterial resistance with similar solubility, framework tunability, and cytotoxicity.

Ruthenium-based drugs have seen a great deal of success in treating a wide class of cancers, with drugs such as NAMI-A [8], NKP1339 [9], and KP1019 [10] seeing phase I of clinical trials, and TLD1433 [11] seeing phase II of clinical trials in treating colorectal cancers. With the prior drugs sharing an imidazole/indazole group and a perchlorinated Ru(III) center, TLD1433 is a Ru(II)-polypyridyl complex containing two 6,6′-dimethyl-2,2′-bipyridine ancillary ligands with and a main α-terthienyl ligand. These anticancer complexes can take on a variety of frameworks, as seen with ruthenium arene phosphaadamantane (RAPTA) complexes, half-sandwich complexes, and the previously mentioned Ru(II)-polypyroidal complexes, which are currently being used in general chemotherapy and photochemotherapy regimens [12]. Recent works by McQuaid et al. have provided an experimental basis for the binding modes of these complexes with both duplex DNA and G-quadruplexes via X-ray Crystallography, and this provides a structural basis for the chemotherapeutic potential of these complexes [13,14].

Other groups have investigated the efficacy of Ruthenium (II) polypyridyl complexes as DNA-binders in chemotherapy and photo-dynamic therapy regimens, such as the Simović group [12,15,16] and the Loftus group [17,18] with their Ru(II) 2,2′:6′,2″-terpyridine (tpy) complexes and ancillary bidentate ligands. These complexes express an exclusively meridional geometry, which has been reported to increase the solubility of Ru(II) polypyridyl drugs in aqueous media [19]. With a similar scaffold, the emphases for these groups are slightly different. The Loftus group has tuned their complexes for drug-delivery systems, with low-lying triplet metal-to-ligand-charge-transfer (^{3}MLCT) and triplet ligand field (^{3}LF) states previously reported to lead to superior photosensitizers [20], whereas the Simović group emphasizes their complexes' innate cytotoxicity in both proteins and cancerous DNA. Although both series of complexes contain axial ligands that allow these drugs to function as monofunctional adducts post-water association, the nitrile group of the Loftus complexes is photolabile and this group is released upon a singlet-triplet (ST) transition, wheras the chlorine ligand in the Simović group's complexes is readily released, forming a Ru(II) aquamet species.

Prior work from our group focused on the experimentally determined quantum yields of the Loftus group to determine if there was a correlation between those values and Ru-NC bond strengths via nitrile dissociation [21]. They concluded that changes in the metal framework, from the triplet excited state to the singlet ground state, precede the breaking of the Ru-NC bond and that complexes with higher quantum yields generally display higher Ru-NC bond strengths and ST splittings. They also observed an inverse relationship between the strength of the Ru-NC bond and the axial portion of the bidentate ligand, as shown in other prior work [22]. As that work primarily focused on the function of these complexes as drug-delivery systems, in this work we focused on the question of: What is the efficacy of this framework to serve as monofunctional adducts, as opposed to drug-delivering agents?

Others have been interested in monofunctional adducts for DNA damage, as prodrugs that form covalent bonds with their target resurge

in popularity [23]. Shown in prior work, these drugs have access to a variety of cellular transport mechanisms, whether it is via iron transporters [24] or human serum albumin (HSA) [25], and a wide array of tunable geometries that vary target-selectivity and photochemical affinity. Shown in Fig. 1 are the complexes observed in this study and their associated guanosine adducts. Noted for their structural similarity, complex 3 contains a bipyridine (bpy) ligand, whereas complex 4 contains a 1,10–phenanthroline (phen) ligand. Complexes 16–18 serve as an extension of complex 3 with modifications to the main scaffold. Complexes 8–15 vary the trend of using aromatic N-heterocycles as ancillary ligands, including acetylacetonate (acac) derivatives and a 2-oxidobenzoate group in complex 15. complexes 13 and 14 subtend this trend by including aminated acac derivatives to determine the significance of incorporating a Ru-O bond in the scaffold. Similar drugs to the scaffold have been noted for both their DNA-binding and photochemical affinity, so bond strength measures were determined for the complexes in both the singlet ground state and first triplet excited state to indicate any changes in the metal framework that would allow for favorable photo-induced transitions.

In this work, DNA-binding affinity was assessed via local vibrational mode force constants k^a derived from the local vibrational mode theory, developed by our group [26,27], complemented with topological analysis of the electronic density using Bader's quantum theory of atoms-in-molecule (QTAIM) [28,29]. We hope to demonstrate in this manuscript the level of detail and chemical intuition local mode analysis (LMA) offers over other methodologies, inspiring the broader community to add LMA to their repertoire.

2. Computational methods

2.1. Local vibrational mode analysis

LMA, originally developed by Konkoli and Cremer [30], has become a versatile tool for extracting important chemical information from vibrational spectroscopy data, often hidden due to the delocalization of normal vibrational modes in polyatomic molecules [31]. Besides pioneering to a new way to analyze vibrational spectra, as shown in the composition of normal mode (CNM) analysis [32] LMA has led to a new quantitative measure of bond strength based on local vibrational mode force constants (k^a) [33]. The underlying theory as well as a comprehensive overview of LMA applications can be found in two recent review articles [26,27].

Rather than directly comparing values of local force constants, it is conventional to associate a bond strength order (BSO) for a series of compounds. This relationship can be described by a generalized Badger rule, as shown from the work of Kraka, et al. [34]

$$\text{BSO n} = a(k^a)^b \tag{1}$$

The constants a and b in Eq. (1) can be determined by two reference compounds with known k^a and the requirement that for a zero k^a the corresponding BSO n value is zero. For this work, using RuH and RuO as reference molecules, the values of those constants were determined to be $a = 0.7441$ and $b = 0.3879$, based on scaled Mayer bond orders [35] (1.0 for the RuH bond and 1.5803 for the RuO bond, respectively) and local mode force constants (2.143 and 6.978 mDyn/Å for RuH and RuO, respectively), calculated at a PBE0/cc-pVTZ/SDD level of theory [21].

2.2. QTAIM analysis

As done in previous work [21] the covalent character of the Ru-N_7 (RuN) and Ru-L_{ax} (RuL) bonds was assessed by the Cremer-Kraka criterion [36,37] analyzing the value of the energy density H_b taken at the bond critical point r_b along the electron density path spanning two atoms in a bond or weak interaction [28,29]. A negative value of H_b indicates the predominately covalent character of the chemical bond or chemical interaction, while a positive value reflects the electrostatic character of the interaction. [36,37]
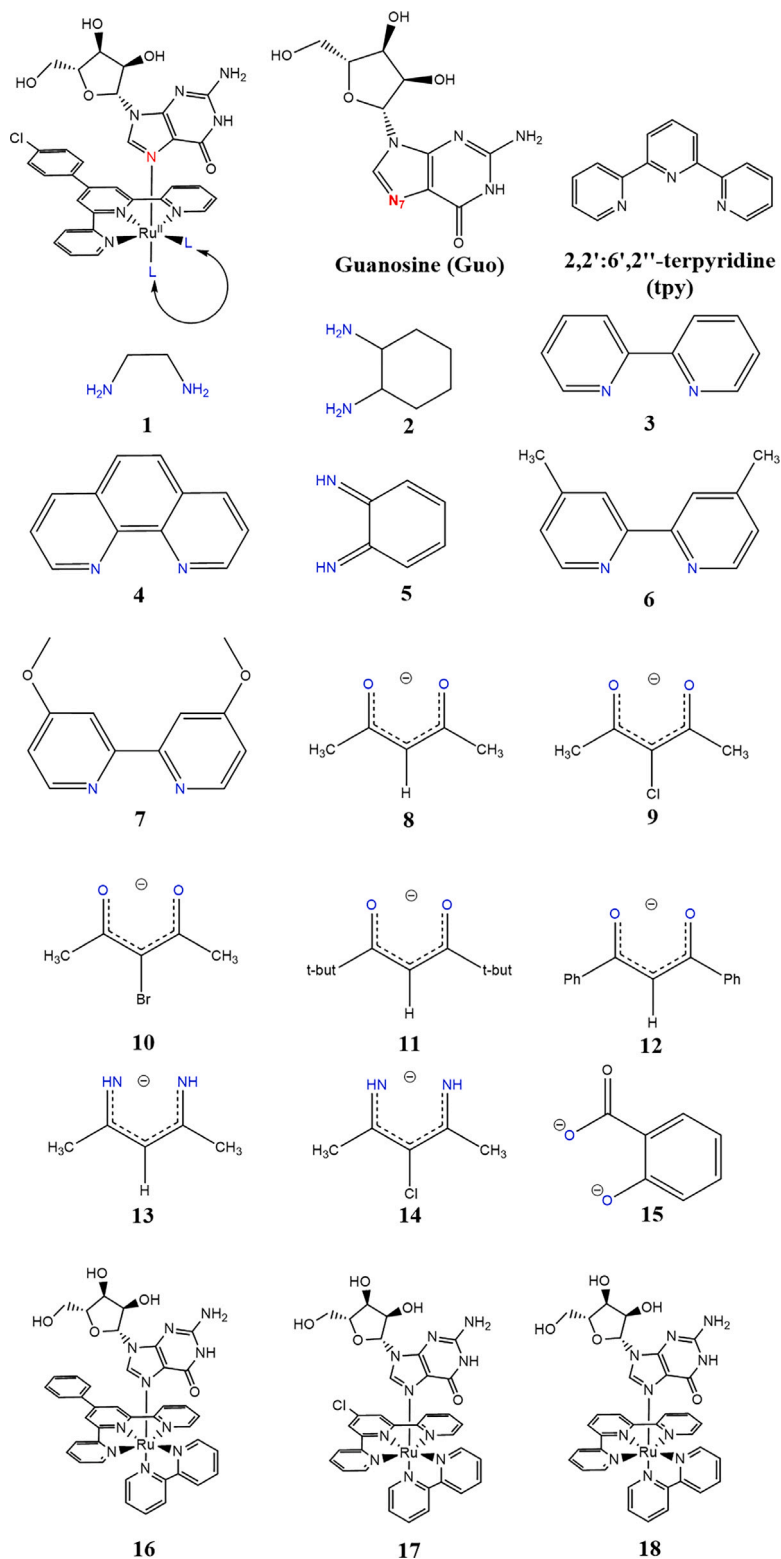
Fig. 1. The series of complexes observed in this study. All complexes, in both singlet ground and triplet excited states, were optimized with a (U)PBE0/cc-pVTZ/SDD level of theory. The charge (n) on the Ru(II) center varies as follows: $n = 0$ for complex 15, $n = +1$ for complexes 8–14, and $n = +2$ for the remaining complexes.

2.3. DFT calculations

All geometry optimizations, frequency calculations, and wave function analyses were performed using Density Functional Theory (DFT) [38] The PBE0 (PBE1PBE) hybrid functional was used, [39] as it has been previously shown to best match experimental results for

methylimidazole complexes [40]. Dunning's and Kendall's cc-pVTZ basis set [41] was used in addition to the Stuggart-Dresden effective core potential (SDD) to account for the relativistic effects seen with second-row transition metals. This effective core potential is a quasi-relativistic *ab initio* pseudo-potential that substitutes the M(Z-28)$^+$ core orbitals and the more optimized GTO valence basis set and the corresponding

Table 1

Table of Local Mode parameters. Bond length q_n (Å), local mode force constant k^a (mdyn/Å), bond strength order BSO, electron density ρ_b (e/Bohr^3), energy density H_b (Har/Bohr^3) at the bond critical point b, and the singlet-triplet (ST) splitting (kcal/mol) for complexes 1–18. (U)PBE0/cc-pVTZ/SDD level of theory.

Complex	Singlet					Triplet					ST splitting
	q_n	k^a	BSO	ρ_b	H_b	q_n	k^a	BSO	ρ_b	H_b	
RuN bond											
1	2.110	1.671	0.908	0.087	−0.018	2.071	1.671	0.908	0.101	−0.028	40.272
2	2.112	1.533	0.878	0.087	−0.018	2.076	1.636	0.901	0.100	−0.027	39.488
3	2.144	1.318	0.828	0.081	−0.015	2.106	1.532	0.878	0.093	−0.023	41.647
4	2.141	1.339	0.833	0.081	−0.015	2.103	1.555	0.883	0.093	−0.023	41.779
5	2.145	1.405	0.849	0.083	−0.017	2.144	1.399	0.848	0.085	−0.019	15.271
6	2.146	1.305	0.825	0.080	−0.014	2.111	1.493	0.869	0.091	−0.022	40.738
7	2.159	1.187	0.795	0.078	−0.014	2.159	1.187	0.795	0.090	−0.021	36.532
8	2.105	1.481	0.867	0.088	−0.019	2.091	1.577	0.888	0.095	−0.023	28.904
9	2.103	1.496	0.870	0.088	−0.019	2.087	1.603	0.894	0.095	−0.024	28.769
10	2.103	1.498	0.870	0.088	−0.019	2.094	1.662	0.906	0.088	−0.011	28.283
11	2.114	1.423	0.853	0.086	−0.018	2.114	1.423	0.853	0.086	−0.018	27.632
12	2.110	1.474	0.865	0.088	−0.020	2.118	1.447	0.859	0.089	−0.021	33.039
13	2.157	1.202	0.799	0.078	−0.014	2.151	1.315	0.827	0.077	−0.007	20.485
14	2.174	1.152	0.786	0.074	−0.011	2.169	1.242	0.809	0.073	−0.004	15.255
15	2.131	1.367	0.840	0.083	−0.016	2.123	1.519	0.875	0.084	−0.021	14.538
16	2.140	1.322	0.829	0.081	−0.015	2.106	1.535	0.879	0.093	−0.023	41.851
17	2.140	1.325	0.830	0.081	−0.015	2.106	1.541	0.880	0.093	−0.023	40.573
18	2.144	1.326	0.830	0.081	−0.015	2.107	1.532	0.878	0.093	−0.023	40.887
RuL bond											
1	2.133	1.532	0.878	0.086	−0.019	2.133	1.532	0.878	0.090	−0.022	
2	2.132	1.514	0.874	0.087	−0.020	2.132	1.514	0.874	0.092	−0.023	
3	2.058	1.949	0.964	0.103	−0.028	2.058	1.949	0.964	0.102	−0.029	
4	2.064	1.880	0.951	0.101	−0.027	2.064	1.880	0.951	0.100	−0.028	
5	1.991	2.097	0.992	0.122	−0.042	1.991	2.097	0.992	0.128	−0.046	
6	2.059	1.975	0.969	0.103	−0.028	2.059	1.975	0.969	0.104	−0.030	
7	2.061	1.967	0.967	0.102	−0.028	2.061	1.967	0.967	0.104	−0.030	
8	2.048	1.961	0.966	0.091	−0.015	2.048	1.961	0.966	0.102	−0.022	
9	2.042	2.009	0.975	0.092	−0.015	2.042	2.009	0.975	0.103	−0.022	
10	2.040	2.026	0.979	0.092	−0.015	2.040	2.026	0.979	0.087	−0.017	
11	2.041	2.031	0.979	0.093	−0.016	2.041	2.031	0.979	0.093	−0.016	
12	2.046	1.914	0.957	0.090	−0.014	2.046	1.914	0.957	0.102	−0.022	
13	2.030	2.265	1.022	0.112	−0.035	2.030	2.265	1.022	0.108	−0.023	
14	2.019	2.346	1.036	0.115	−0.037	2.019	2.346	1.036	0.111	−0.026	
15	2.011	2.191	1.009	0.105	−0.025	2.011	2.191	1.009	0.105	−0.030	
16	2.058	1.947	0.964	0.102	−0.028	2.058	1.947	0.964	0.103	−0.029	
17	2.059	1.944	0.963	0.103	−0.028	2.059	1.944	0.963	0.102	−0.029	
18	2.060	1.943	0.963	0.103	−0.028	2.060	1.943	0.963	0.102	−0.029	

spin–orbit coupling operator [42]. For all triplet state calculations, unrestricted DFT was applied [43]. DFT calculations were carried out with Gaussian 16 [44]. An UltraFine integration grid was used in all DFT calculations [45]. Local mode force constants were calculated using the program package LModeA [46]. QTAIM was performed with the AIMALL program, and Mayer bond orders were calculated with Gaussian 16.

2.4. Bond dissociation energies

Bond dissociation energies (E_{diss}) for the RuN bond were determined for the following process:

$$Ru(tpy)(L)^{n+} \cdots Guo \rightarrow Ru(tpy)(L)^{(n-1)+} + Guo^+ \tag{2}$$
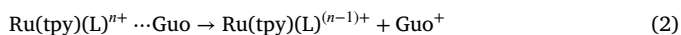
where the following equation determined the energies [47]:

$$E_{diss} = E(Ru(tpy)(L)^{(n-1)+}) + E(Guo^+) - E(Ru(tpy)(L)^{n+} \cdots Guo) \tag{3}$$

Minimum energies were determined for the monomers and dimer complex using a PBE0/cc-pVTZ/SDD level of theory for both singlet and triplet states using Gaussian 16. Unrestricted DFT was applied for all triplet state calculations.

3. Results and discussion

3.1. DNA/guanosine affinity

Local mode force constants and related BSO n values were used to determine the relative binding affinity of these complexes with guanine derivatives at the N_7 position and their axial ligand L_{ax}. Table 1 summarizes the data collected in this analysis, with the singlet-triplet (ST) splitting for each complex shown on the right and the bond's electronic density ρ_b shown for comparison to the energy density H_b at the bond critical point. Local mode force constants and their corresponding Mayer bond orders were determined using the generalized Badger rule, Fig. 2 demonstrates this power relationship for the complexes and their axial ligand in both the singlet ground and first triplet excited states, with their associated BSO n values plotted against one another. Fig. 2a and b correspond to the plots of the Ru-N_7 bond in both the singlet ground state and first triplet excited state. The BSO n values for Fig. 2a range from 0.786 to 0.908, while for Fig. 2b, these values range from 0.795 to 0.908. These values tend towards higher local force constants and BSO n values when excited to the first triplet excited state, with a smaller variance separating these values. The complexes with the lowest BSO n values would be complexes 7, 13, and 14, while those with the highest BSO n values would be complexes 1, 2, and 10. While the exact order of these bond strengths varies from the singlet to the triplet state, the overall trend is preserved in the RuN bond with more bulky, aromatic ligands and electron-withdrawing ligands displaying smaller BSO n values while more flexible, electron-donating ligands displaying higher BSO n values. These plots are best viewed in comparison with plots displaying the local mode force constants for the Ru-L_{ax} (RuL) bond, where it is evident that on average the local mode force constants and BSOs vary inversely across the complexes for the RuN and RuL bonds.
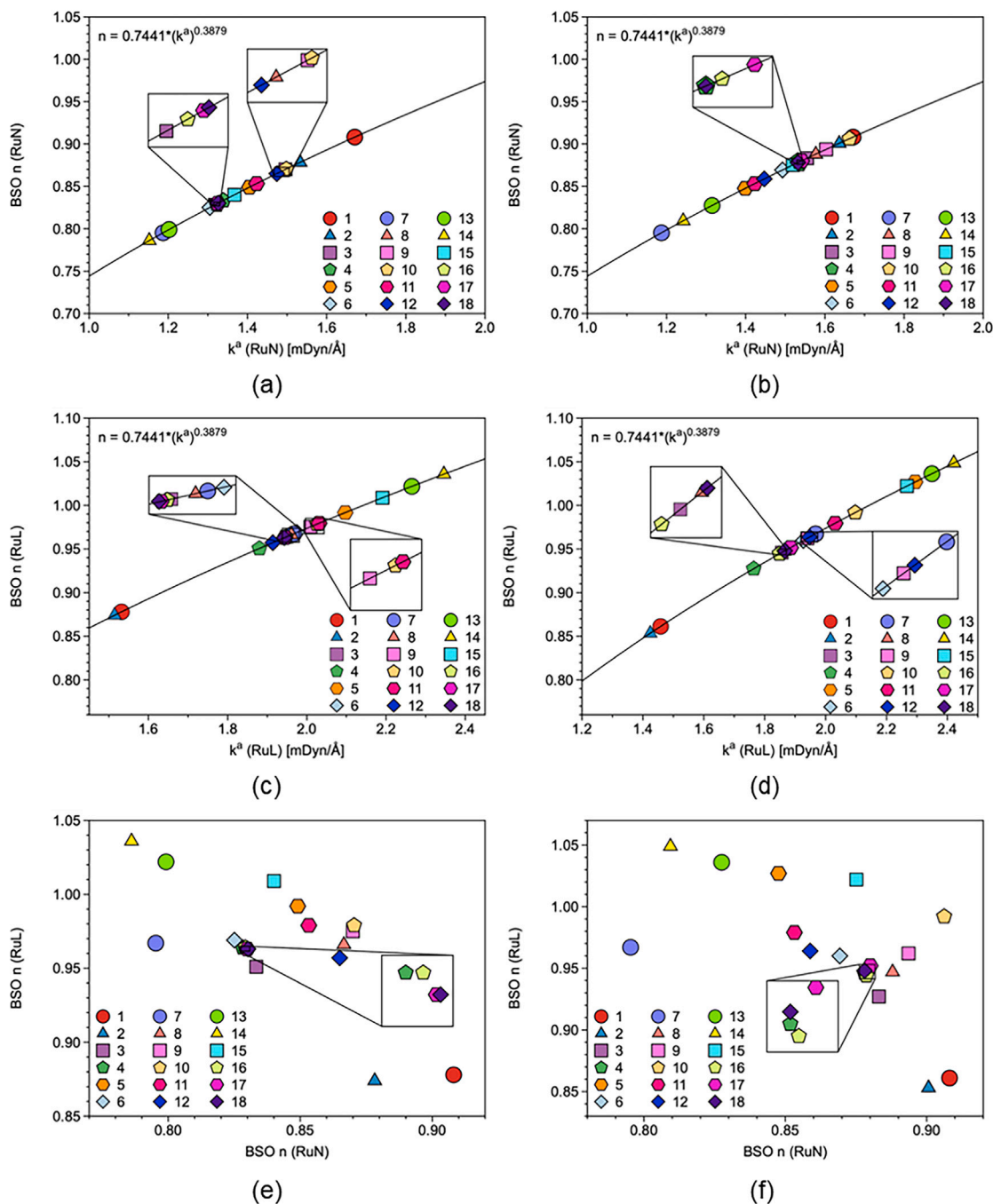
Fig. 2. BSO n values of all RuN bonds (singlet and triplet states) and values of all RuL bonds (singlet and triplet states) obtained with the power relationship BSO n = 0.7441(kᵃ)^0.3879, calculated at the (U)PBE0/cc-pVTZ/SDD level of theory. See text and Eq. (1) for the derivation of the power relationship. (a) RuN Singlet, (b) RuN Triplet, (c) RuL Singlet, (d) RuL Triplet, (e) Cross-correlation of RuN and RuL BSO n Singlet, (f) Cross-correlation of RuN and RuL BSO n Triplet.

3.2. Ligand affinity

Fig. 2c and d correspond to the plots of the Ru-L_{ax} bond in the singlet ground state and first triplet excited state. The BSO n values for Fig. 2c range from 0.874 to 1.036, while the BSO n values for Fig. 2d range from 0.853 to 1.049. While the BSO n values tend to be slightly higher in the excited state for the RuN bond, the values in the triplet excited state display a wider range of values, some smaller and some higher. This broadened range contrasts the trend observed for the RuN bond where the BSO n values in the triplet excited state tend to cluster more tightly than the singlet ground state. Fig. 2e and f correspond to the BSO n values for the RuN and RuL bonds plotted in the singlet ground state and triplet excited state, respectively. The trend described

before is then found here when comparing these plots, as for the singlet state there lies greater variability in the RuN BSO n values, whereas in the triplet state there lies greater variability in the RuL BSO n values. This could correspond more broadly to a shift in the electronic density of the singlet ground state that would be expected when transitioning to a triplet excited state. These values generally correspond with a negative linear correlation, where the bond strength of the RuN bond can be diminished by the strengthening of the RuL bond.

3.3. The Cremer-Kraka criterion and critical energy density

While this inverse relationship between local mode force constants and BSO n values for the different bonds confirms what was originally
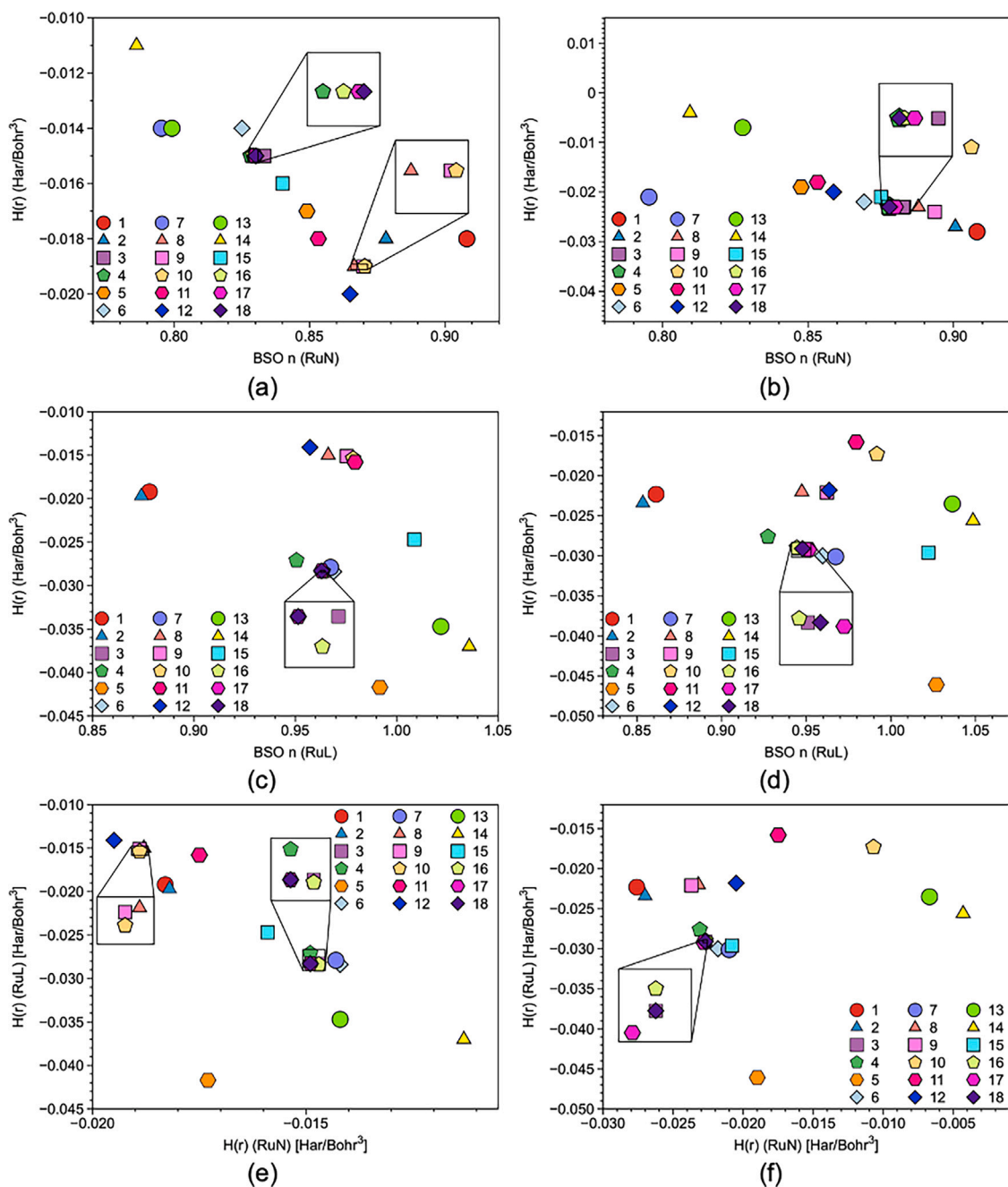
Fig. 3. Correlation between energy density H_b and BSO n values for RuN bonds (singlet and triplet states) and for RuL bonds (singlet and triplet states) calculated at the (U)PBE0/cc-pVTZ/SDD level of theory. (a) RuN Singlet, (b) RuN Triplet, (c) RuL Singlet, (d) RuL Triplet, (e) Cross-correlation of RuN and RuL H_b Singlet, (f) Cross-correlation of RuN and RuL H_b Triplet.

expected for these complexes, this trend also be described in terms of changes in the energy density at the bond critical point H_b, Fig. 3 compares the H_b values for each bond in the singlet and triplet state, and illustrates the correlations between energy densities of the two bonds. As all electronic density values are negative, it can be confirmed by the Cremer-Kraka criterion that each of these interactions corresponds to a covalent bond [36,37]. Similar to the prior figure, Fig. 3a and b correspond to the RuN bond in the singlet and triplet state. The bond energy density values for Fig. 3a range from −0.0195 to −0.0113 Har/Bohr^3, whereas the values in 3b range from −0.0276 to −0.0043 Har/Bohr^3. A similar pattern is noted for the bond density of the triplet state that was observed for the local mode force constants, in that the energy density of the bond critical points of the RuN bond is not greatly affected by the choice of ligand for this system. The

slight differences in these densities correspond with the trend that more flexible, electron-donating ligands strengthen the energy density of the RuN bond. However, the opposite trend noted for the RuL bond is arguably not maintained for its energy densities. The associated Fig. 3c and d would indicate this bond is highly delocalized over the density. While similar ligands cluster together in these plots, the correlation among these densities is not as evident as in the figures above. The following plots presented in Fig. 3e and f serve to illustrate these relationships better, displaying the H_b for the RuN bond and the RuL bond for both the singlet and triplet states. While a negative linear trend can be seen for the singlet state bonds, this trend is obscured for the triplet state bonds. A consistent trend in visualizing these complexes in the triplet state is the tight proximity the complexes keep with one another, where the RuL bonds appear to vary more than the RuN
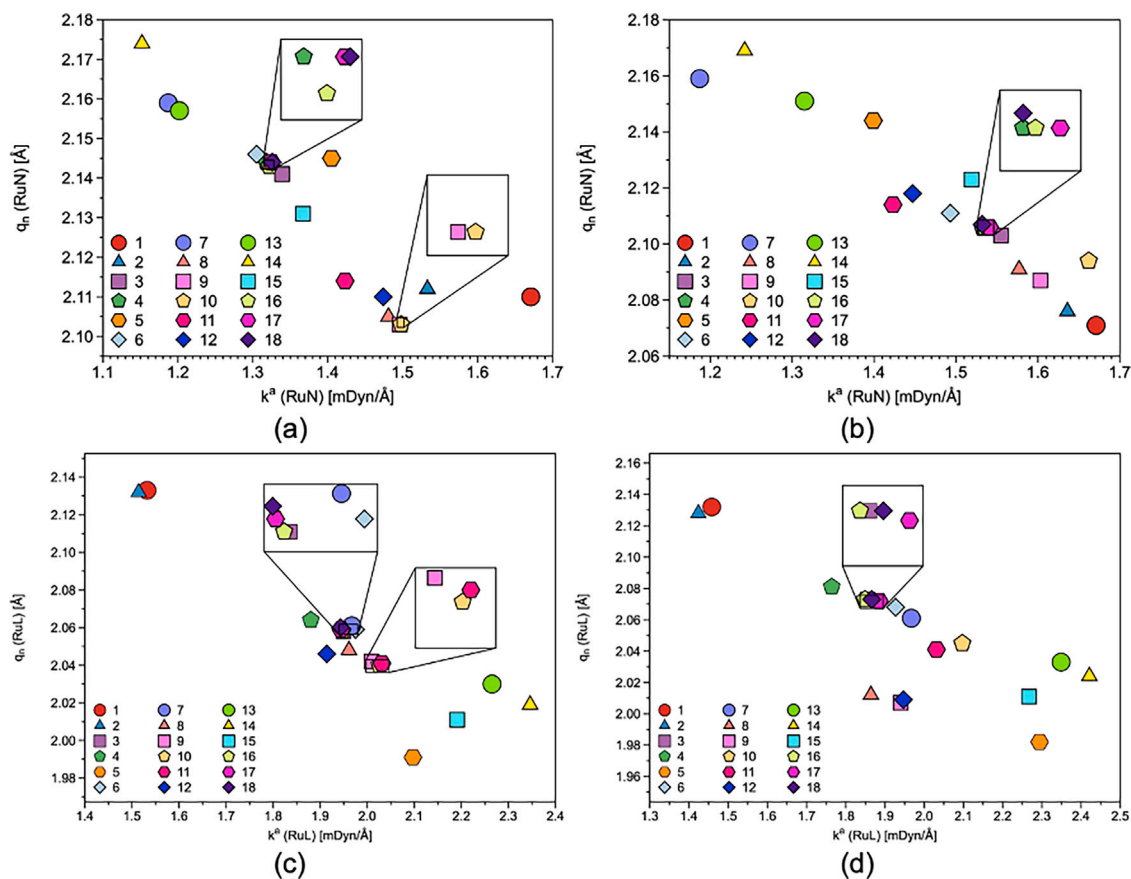
Fig. 4. Bond lengths and k^a values for RuN bonds (singlet and triplet states) and RuL bonds (singlet and triplet states) calculated at the (U)PBE0/cc-pVTZ/SDD level of theory. (a) RuN Singlet, (b) RuN Triplet, (c) RuL Singlet, (d) RuL Triplet.

bonds. This implies some tunability in this scaffold with similar RuN affinity providing some variability in the energy density attributed to RuL affinity. While comparing the energy density $\mathbf{H_b}$ with BSO n values provides us with similar energetic information in describing these complexes, comparing bond distances and their BSO n values add a needed geometric component to this analysis in extracting how this differential energy character displays itself across the scaffold.

3.4. Bond length vs. bond strength

Fig. 4 displays the bond lengths of all complexes compared with their BSO n values. Fig. 4a and b correspond to the RuN bond in the singlet and triplet state, with bond lengths varying from 2.103 to 2.174 Å in the singlet state and from 2.071 to 2.169 Å in the triplet state. The smallest bond lengths are associated with complexes 9 and 10 in the singlet state, and this is unsurprising as these ligands are the most electron-rich with bulky halogen substituents and by providing density to the RuL bond reinforce the RuN bond. The smallest bond lengths in the triplet state correspond to complexes 1 and 2, which are the most electron-neutral ligands so great shifts in the energy density of the scaffold would not be anticipated in shifting to a triplet excited state. The largest bond lengths in both singlet and triplet states correspond to complexes 7, 13, and 14, and this is expected as these ligands share added traits of the polypyridyl scaffold with an N-linking aromatic structure, likely isoelectronic to the other portions of the scaffold. Fig. 4c and d correspond to the RuL bond in the singlet and triplet state, with bond distances varying from 1.991 to 2.133 Å in the singlet state and from 1.982 to 2.132 Å in the triplet state. These plots serve to substantiate the inverse proportionality of the strength/distance of the RuN bond and the RuL bond, with the shortest RuL bonds generally

displaying longer RuN bonds and the complexes with the longest RuN bonds generally displaying shorter RuL bonds.

Four main clusters appear from these plots: the first simply being complexes 1 and 2, the next being complexes 5, 13, 14, and 15, with complexes 3, 16, 17, and 18 forming the third cluster, and the final cluster being loosely attributed with all other complexes in this work. This first cluster can be described as complexes with great RuN affinity with poor RuL affinity. This can be justified by the electronically neutral nature of these ligands with a lack of π-conjugation being unable to withdraw electronic density from the RuN bond to then strengthen the RuL bond. The second cluster, with complexes 5, 13, 14, and 15, tends to display a lower affinity with the RuN bond and a higher affinity with the RuL bond, and this provides some indication that rigid, aromatic ligands provide sufficient density in their RuL bonds which fails to enhance the density of the RuN bond. Not only does this analysis provide an indication of how to strengthen the RuN bond, but it similarly shows ways to weaken this bond for variable selectivity. The third cluster demonstrates how changes in the main scaffold affect the RuN and RuL bonds, with 3 and 16, each possessing a phenyl group at the 4' position, displaying weaker RuN bonds while 17 and 18, lacking a phenyl group at the 4' position, displaying weaker RuL bonds. The remaining cluster of complexes contains ligands with a mix of electronic properties that could serve to abet the weaker RuN affinity seen in cluster 2 with the heightened RuN affinity of cluster 1 with acac aromatic ligands.

3.5. Bond dissociation energies

To complement this analysis with other measures of bond strength, bond dissociation energies were calculated for the cleavage of the RuN bond, and these results are shown in Table 2. The bond cleavage
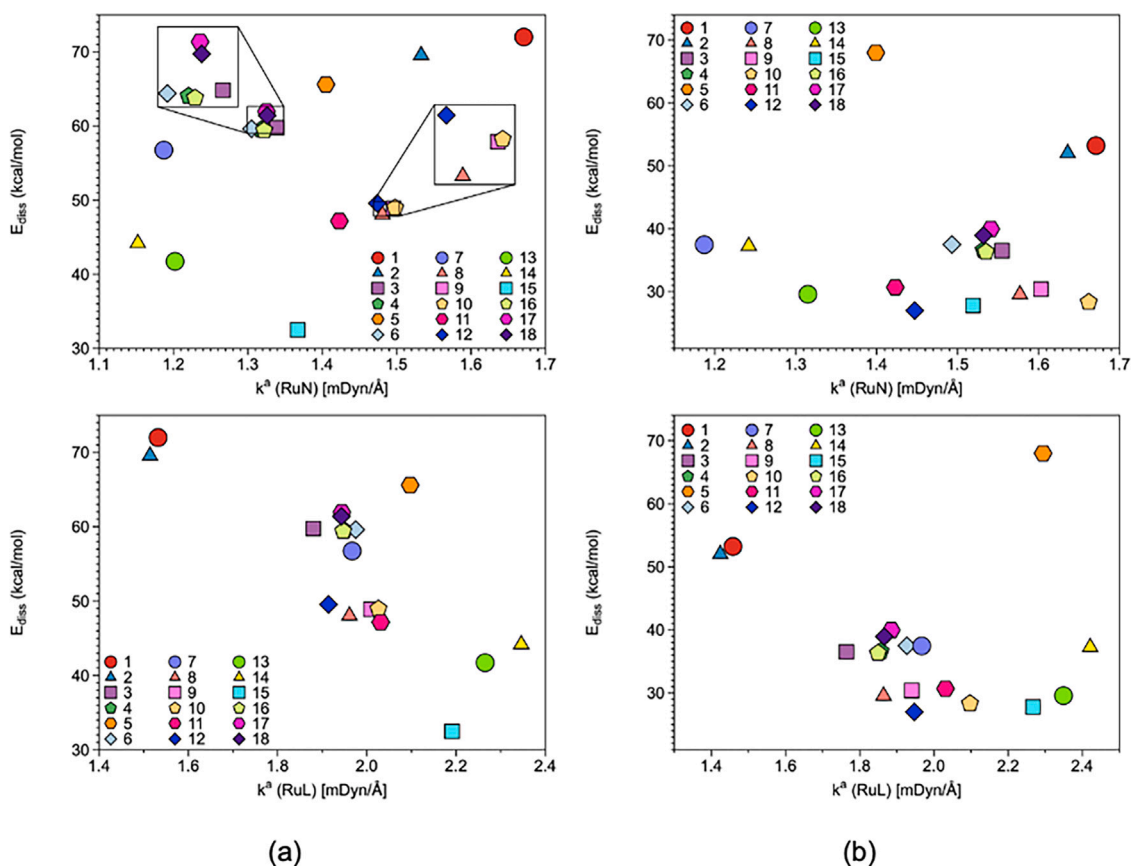
Fig. 5. Bond dissociation energies (E_{diss}) and BSO n values for RuN bonds (singlet and triplet states) and RuL bonds (singlet and triplet states) calculated at the (U)PBE0/cc-pVTZ/SDD level of theory. (a) Singlet, (b) Triplet.

Table 2
Bond Dissociation Energies (E_{diss}) for the RuN bond in complexes 1–18, details concerning these calculations can be found in the Computational Methods section. Energies are listed in units of kcal/mol.

Complex	Singlet	Triplet
1	72.002	53.223
2	69.552	52.008
3	59.503	36.592
4	59.760	36.513
5	65.611	67.977
6	59.617	37.497
7	56.744	37.474
8	48.044	29.576
9	48.900	30.411
10	48.964	28.340
11	47.168	30.696
12	49.562	27.007
13	41.728	29.596
14	44.188	37.274
15	32.493	27.805
16	59.414	36.331
17	61.942	39.964
18	61.398	38.942

was considered in terms of a heterolytic cleavage, where the Ru (II) center stabilizes an electron from Guo. These energies are noticeably large, ranging from 32.493 to 72.002 kcal/mol in the singlet state and 27.007 to 53.223 kcal/mol in the triplet state, accounting for the outlier observed with complex 5 having a bond dissociation energy of 67.977 kcal/mol. These energies similarly follow the trend seen in the ST splittings, except for complex 5 which displays an ST splitting of 15.271 kcal/mol. From purely an energetic standpoint, it is unclear why complex 5 displays one of the highest E_{diss}s across the series, and yet

it displays one of the lowest ST splittings. Complex 5 presents itself as unaffected by an ST transition as the critical energy density, BSO n values, and bond lengths are narrowly differing from the ground state to the excited state. Shown in Fig. 5 are these energies plotted against their respective local force constants for the RuN and RuL bonds in the singlet and triplet states. These plots illustrate that the binding affinity of these complexes is directly related to the bond strength of their ancillary ligands as shown with our prior analysis; however, these triplet state dissociation energies do not vary proportionally with the calculated triplet state local force constants.

This lack of proportionality is related to the small variance in these energies, especially noted in Fig. 5d, which likely corresponds to the geometric differences of the complexes in their first triplet excited states sharing more similar features than in their geometries in the singlet ground state. Using the local descriptors constructed in the methodology of LMA, mitigates potential pitfalls in using global descriptors, such as bond dissociation energies, to define measures of binding affinity and interaction strengths when more sophisticated tools are available.

4. Conclusions and outlook

In summary, the inverse relationship between RuN and RuL bonds indicates binding selectivity for this scaffold. Additionally, the inverse relationship between RuN bonds and activation energies provides another dimension of tunability that aligns with the observations made through the local mode picture. Furthermore, complexes 8–12 exhibit electronic properties that impart sufficient density to the RuN bond, enabling binding with guanine derivatives and resulting in lower activation energies.

Although complex 1 demonstrates the strongest Guo binding affinity, the Guo binding affinities among the 18 complexes do not show

significant differences. However, complexes 13, 14, and 15 exhibit the strongest ligand affinity. These compounds are also notable for their high photochemical affinity, as confirmed by their singlet-triplet splitting energies. Therefore, we recommend further investigating complexes 13, 14, and 15 to develop photoactive Ru-based cancer drugs, while complexes 8–12 provide the greatest flexibility in a tunable scaffold with modifiable selectivity for DNA. Future works could emphasize using these complexes as major-groove binders and DNA intercalators as mentioned in works of Simović, et al.

CRediT authorship contribution statement

Hunter La Force: Conceptualization, Execution, Visualization, First draft writing. **Elfi Kraka:** Conceptualization, Evaluation, Editing, Supervision.

Declaration of competing interest

The authors declare the following financial interests/personal relationships which may be considered as potential competing interests: Elfi Kraka's report was provided by Southern Methodist University. Elfi Kraka reports a relationship with Southern Methodist University that includes: employment. There are no additional relationships or activities to declare.

Data availability

Data will be made available on request.

Appendix A. Supplementary data

Supplementary material related to this article can be found online at https://doi.org/10.1016/j.cplett.2023.140733. Cartesian coordinates for the complexes can be found in their singlet ground and first triplet excited states.

References

[1] R.L. Siegel, K.D. Miller, N.S. Wagle, A. Jemal, Cancer statistics, 2023, CA: Cancer J. Clin. 73 (2023) 17–48.

[2] P.J. Dyson, G. Sava, Metal-based antitumour drugs in the post genomic era, Dalton Trans. (2006) 1929–1933.

[3] T.C. Johnstone, K. Suntharalingam, S.J. Lippard, The next generation of platinum drugs: Targeted Pt(II) agents, nanoparticle delivery, and Pt(IV) prodrugs, Chem. Rev. 116 (2016) 3436–3486.

[4] C. Polonyi, A. Alshiekh, L.A. Sarsam, M. Clausén, S.K.C. Elmroth, Cisplatin-induced duplex dissociation of complementary and destabilized short GG-containing duplex RNAs, Dalton Trans. 43 (2014) 11941–11949.

[5] A. Barbanente, A. Galliani, R.M. Iacobazzi, A. Lasorsa, M.I. Nardella, A. Pennetta, N. Margiotta, F. Arnesano, Interaction of copper trafficking proteins with the platinum anticancer drug kiteplatin, ChemMedChem 17 (2022) e202100593.

[6] P.M. Bruno, Y. Liu, G.Y. Park, J. Murai, C.E. Koch, T.J. Eisen, J.R. Pritchard, Y. Pommier, S.J. Lippard, M.T. Hemann, A subset of platinum-containing chemotherapeutic agents kills cells by inducing ribosome biogenesis stress, Nature Med. 23 (2017) 461–471.

[7] L. Galluzzi, L. Senovilla, I. Vitale, J. Michels, I. Martins, O. Kepp, M. Castedo, G. Kroemer, Molecular mechanisms of cisplatin resistance, Oncogene 31 (2012) 1869–1883.

[8] J.M. Rademaker-Lakhai, D. van den Bongard, D. Pluim, J.H. Beijnen, J.H.M. Schellens, A phase I and pharmacological study with imidazolium-trans-DMSO-imidazole-tetrachlororuthenate, a novel ruthenium anticancer agent, Clin. Cancer Res. 10 (2004) 3717–3727.

[9] R. Trondl, P. Heffeter, C.R. Kowol, M.A. Jakupec, W. Berger, B.K. Keppler, NKP-1339, the first ruthenium-based anticancer drug on the edge to clinical application, Chem. Sci. 5 (2014) 2925–2932.

[10] C.G. Hartinger, M.A. Jakupec, S. Zorbas-Seifried, M. Groessl, A. Egger, W. Berger, H. Zorbas, P.J. Dyson, B.K. Keppler, KP1019, a new redox-active anticancer agent – preclinical development and results of a clinical phase I study in tumor patients, Chem. Biodivers. 5 (2008) 2140–2155.

[11] S. Monro, K.L. Colón, H. Yin, J.I. Roque, P. Konda, S. Gujar, R.P. Thummel, L. Lilge, C.G. Cameron, S.A. McFarland, Transition metal complexes and photodynamic therapy from a tumor-centered approach: Challenges, opportunities, and highlights from the development of TLD1433, Chem. Rev. 119 (2019) 797–828.

[12] A. Řilak Simović, R. Masnikosa, I. Bratsos, E. Alessio, Chemistry and reactivity of ruthenium(II) complexes: DNA/protein binding mode and anticancer activity are related to the complex structure, Coord. Chem. Rev. 398 (2019) 113011.

[13] K.T. McQuaid, C.J. Cardin, The eyes have it: Using X-ray crystallography to determine the binding modes of medically relevant ruthenium/DNA complexes, in: Advances in Inorganic Chemistry, Vol. 75, 2020, pp. 393–424.

[14] K.T. McQuaid, S. Takahashi, L. Baumgaertner, D.J. Cardin, N.G. Paterson, J.P. Hall, N. Sugimoto, C.J. Cardin, Ruthenium polypyridyl complex bound to a unimolecular chair-form G-quadruplex, J. Am. Chem. Soc. 144 (2022) 5956–5964.

[15] M.M. Milutinović, A. Řilak, I. Bratsos, O. Klisurić, M. Vraneš, N. Gligorijević, S. Radulović, Ž.D. Bugarčić, New 4-(4-chlorophenyl)-2,2':6',2''-terpyridine ruthenium(II) complexes: Synthesis, characterization, interaction with DNA/BSA and cytotoxicity studies, J. Inorg. Biochem. 169 (2017) 1–12.

[16] M. Međedović, A.Ř. Simović, D. Ćocić, L. Senft, S. Matić, D. Todorović, S. Popović, D. Baskić, B. Petrović, New ruthenium(II) complexes with quinone diimine and substituted bipyridine as inert ligands: synthesis, characterization, mechanism of action, DNA/HSA binding affinity and cytotoxic activity, Dalton Trans. 52 (2023) 1323–1344.

[17] L.M. Loftus, J.K. White, B.A. Albani, L. Kohler, J.J. Kodanko, R.P. Thummel, K.R. Dunbar, C. Turro, New Ru(II) complex for dual activity: Photoinduced ligand release and $^1O_2$ production, Chem. Eur. J. 22 (2016) 3704–3708.

[18] L.M. Loftus, K.F. Al-Afyouni, T.N.J. Rohrabaugh, J.C. Gallucci, C.E. Moore, J.J. Rack, C. Turro, Unexpected role of Ru(II) orbital and spin contribution on photoinduced ligand exchange: New mechanism to access the photodynamic therapy window, J. Phys. Chem. C 123 (2019) 10291–10299.

[19] P.L. Chiu, H.M. Lee, Chemistry of the PCNHCP ligand: silver and ruthenium complexes, facial/meridional coordination, and catalytic transfer hydrogenation, Organometallics 24 (2005) 1692–1702.

[20] A. Cotic, I. Ramírez-Wierzbicki, G.E. Pieslinger, B.M. Aramburu-Trošelj, A. Cadranel, Ligand field states dominate excited state decay in trans-[Ru(py)4Cl2] MLCT chromophores, Inorg. Chim. Acta 518 (2021) 120246.

[21] M. McCutcheon, M. Freindorf, E. Kraka, Bonding in nitrile photo–dissociating ruthenium drug candidates – A local vibrational mode study, J. Chem. Phys. 157 (2022) 014301–1–014301–15.

[22] M. Freindorf, E. Kraka, Critical assessment of the FeC and CO bond strength in carboxymyoglobin - A QM/MM local vibrational mode study, J. Mol. Model. 26 (2020) 281–1–281–15.

[23] F. Sutanto, M. Konstantinidou, A. Dömling, Covalent inhibitors: a rational approach to drug discovery, RSC Med. 11 (2020) 876–884.

[24] M. Klajner, C. Licona, L. Fetzer, P. Hebraud, G. Mellitzer, M. Pfeffer, S. Harlepp, C. Gaiddon, Subcellular localization and transport kinetics of ruthenium organometallic anticancer compounds in living cells: A dose-dependent role for amino acid and iron transporters, Inorg. Chem. 53 (2014) 5150–5158.

[25] Y. Zhang, A. Ho, J. Yue, L. Kong, Z. Zhou, X. Wu, F. Yang, H. Liang, Structural basis and anticancer properties of ruthenium-based drug complexed with human serum albumin, Eur. J. Med. Chem. 86 (2014) 449–455.

[26] E. Kraka, M. Quintano, H.W. La Force, J.J. Antonio, M. Freindorf, The local vibrational mode theory and its place in the vibrational spectroscopy arena, J. Phys. Chem. A 126 (2022) 8781–8900.

[27] E. Kraka, W. Zou, Y. Tao, Decoding chemical information from vibrational spectroscopy data: Local vibrational mode theory, WIREs: Comput. Mol. Sci. 10 (2020) 1480.

[28] R.F.W. Bader, Atoms in Molecules: A Quantum Theory, (Clarendon Press), 1994.

[29] P.L. Popelier, Atoms in Molecules: An Introduction, Prentice Hall, 2000.

[30] Z. Konkoli, D. Cremer, A new way of analyzing vibrational spectra. I. Derivation of adiabatic internal modes, Int. J. Quantum Chem. 67 (1998) 1–9.

[31] E.B. Wilson, J.C. Decius, P.C. Cross, Molecular Vibrations: The Theory of Infrared and Raman Vibrational Spectra, McGraw-Hill, New York, 1955, pp. 59–136, 1955.

[32] N. Verma, Y. Tao, W. Zou, X. Chen, X. Chen, M. Freindorf, E. Kraka, A critical evaluation of vibrational stark effect (VSE) probes with the local vibrational mode theory, Sensors 20 (2020) 2358.

[33] W. Zou, D. Cremer, C_2 in a box: Determining its intrinsic bond strength for the $X^1\Sigma_g^+$ ground state, Chem. Eur. J. 22 (2016) 4087–4097.

[34] E. Kraka, J.A. Larsson, D. Cremer, Generalization of the badger rule based on the use of adiabatic vibrational modes, in: J. Grunenberg (Ed.), Computational Spectroscopy, Wiley, New York, 2010, pp. 105–149.

[35] A.J. Bridgeman, G. Cavigliasso, L.R. Ireland, J. Rothery, The mayer bond order as a tool in chemistry, J. Chem. Soc. Dalton Trans. (2001) 2095–2108.

[36] D. Cremer, E. Kraka, Chemical bonds without bonding electron density? Does the difference electron-density analysis suffice for a description of the chemical bond? Angew. Chem. Int. Edn 23 (1984) 627–628.

[37] D. Cremer, E. Kraka, A description of the chemical bond in terms of local properties of electron density and energy, Croatica Chem. Acta 57 (1984) 1259–1281.

[38] N. Mardirossian, M. Head-Gordon, Thirty years of density functional theory in computational chemistry: An overview and extensive assessment of 200 density functionals, Mol. Phys. 115 (2017) 2315–2372.

[39] C. Adamo, V. Barone, Toward reliable density functional methods without adjustable parameters: The PBE0 model, Chem. Phys. 110 (1999) 6158–6170.

[40] G. Li, L. Chen, X. Wang, L. Wu, X. Jie, J. Chen, Electronic structures, DNA-binding, SAR, and spectral properties of ruthenium methylimidazole complexes $[Ru(MeIm)_4L]^{2+}$ (L = iip, tip, 2ntz), Chin. J. Chem. Phys. 27 (2014) 159–167.

[41] R.A. Kendall, T.H. Dunning, R.J. Harrison, Electron affinities for the first-row atoms revisited. Systematic basis sets and wave functions, J. Chem. Phys. 96 (1992) 6796–6806.

[42] D. Andrae, U. Haeussermann, M. Dolg, H. Stoll, H. Preuss, Energy-adjusted ab initio pseudopotentials for the second and third row transition elements, Theor. Chim. Act. 77 (1990) 123–141.

[43] P. Tarakeshwar, K.S. Kim, E. Kraka, D. Cremer, Structure and stability of fluorine-substituted benzene-argon complexes: The decisive role of exchange-repulsion and dispersion interactions, J. Chem. Phys. 115 (2001) 6018–6029.

[44] M.J. Frisch, G.W. Trucks, H.B. Schlegel, G.E. Scuseria, M.A. Robb, J.R. Cheeseman, G. Scalmani, V. Barone, G.A. Petersson, H. Nakatsuji, X. Li, M. Caricato, A.V. Marenich, J. Bloino, B.G. Janesko, R. Gomperts, B. Mennucci, H.P. Hratchian, J.V. Ortiz, A.F. Izmaylov, J.L. Sonnenberg, D. Williams-Young, F. Ding, F. Lipparini, F. Egidi, J. Goings, B. Peng, A. Petrone, T. Henderson, D. Ranasinghe, V.G. Zakrzewski, J. Gao, N. Rega, G. Zheng, W. Liang, M. Hada, M. Ehara, K. Toyota, R. Fukuda, J. Hasegawa, M. Ishida, T. Nakajima, Y. Honda, O. Kitao, H. Nakai, T. Vreven, K. Throssell, J.A. Montgomery, J.E. Peralta, F. Ogliaro, M.J. Bearpark, J.J. Heyd, E.N. Brothers, K.N. Kudin, V.N. Staroverov, T.A. Keith, R. Kobayashi, J. Normand, K. Raghavachari, A.P. Rendell, J.C. Burant, S.S. Iyengar, J. Tomasi, M. Cossi, J.M. Millam, M. Klene, C. Adamo, R. Cammi, J.W. Ochterski, R.L. Martin, K. Morokuma, O. Farkas, J.B. Foresman, D.J. Fox, Gaussian16 Revision C.01, Gaussian Inc., Wallingford CT, 2016.

[45] J. Gräfenstein, D. Cremer, Efficient DFT integrations by locally augmented radial grids, J. Chem. Phys. 127 (2007) 164113.

[46] W. Zou, Y. Tao, M. Freindorf, M.Z. Makoś, N. Verma, D. Cremer, E. Kraka, Local Vibrational Mode Analysis (LModeA), Computational and Theoretical Chemistry Group (CATCO), Southern Methodist University, Dallas, TX, USA, 2023.

[47] S.J. Blanksby, G.B. Ellison, Bond dissociation energies of organic molecules, Acc. Chem. Res. 36 (2003) 255–263.